

An equivalent source method for modelling the global lithospheric magnetic field

Livia Kother, Magnus D. Hammer, Christopher C. Finlay and Nils Olsen

Division of Geomagnetism, Technical University of Denmark - DTU Space, Kgs. Lyngby, Denmark. E-mail: livia@space.dtu.dk

Accepted 2015 July 27. Received 2015 July 23; in original form 2015 February 24

SUMMARY

We present a new technique for modelling the global lithospheric magnetic field at Earth's surface based on the estimation of equivalent potential field sources. As a demonstration we show an application to magnetic field measurements made by the CHAMP satellite during the period 2009–2010 when it was at its lowest altitude and solar activity was quiet. All three components of the vector field data are utilized at all available latitudes. Estimates of core and large-scale magnetospheric sources are removed from the measurements using the CHAOS-4 model. Quiet-time and night-side data selection criteria are also employed to minimize the influence of the ionospheric field. The model for the remaining lithospheric magnetic field consists of magnetic equivalent potential field sources (monopoles) arranged in an icosahedron grid at a depth of 100 km below the surface. The corresponding model parameters are estimated using an iteratively reweighted least-squares algorithm that includes model regularization (either quadratic or maximum entropy) and Huber weighting. Data error covariance matrices are implemented, accounting for the dependence of data variances on quasi-dipole latitude. The resulting equivalent source lithospheric field models show a degree correlation to MF7 greater than 0.7 out to spherical harmonic degree 100. Compared to the quadratic regularization approach, the entropy regularized model possesses notably lower power above degree 70 and a lower number of degrees of freedom despite fitting the observations to a very similar level. Advantages of our equivalent source method include its local nature, the possibility for regional grid refinement and the production of local power spectra, the ability to implement constraints and regularization depending on geographical position, and the ease of transforming the equivalent source values into spherical harmonics.

Key words: Inverse theory; Magnetic anomalies: modelling and interpretation; Magnetic field; Satellite magnetics.

1 INTRODUCTION

The magnetic investigation of the lithosphere, covering the Earth's crust and upper mantle, is of great importance for many aspects of Earth science, for example, plate tectonics (Molnar 1988), ocean ridge spreading, lithospheric thickness (Langel 1998) and historical meteorite impacts (Plado *et al.* 2000). Since the era of space missions, lithospheric magnetic field modelling techniques are also applicable to the investigation of other objects of our solar system, including Mars, Mercury and the Moon (Ness 1979; Connerney *et al.* 1999; Langlais *et al.* 2004; Whaler & Purucker 2005; Purucker & Nicholas 2010). Furthermore, lithospheric field maps play a significant role in the orientation of subsurface drilling devices (Inglis 1987).

In a source-free region, the geomagnetic field potential may be represented by harmonic functions, which are solutions of the Laplace equation. The most widely used functions for global geomagnetic field modelling are spherical harmonics (SH). However, several studies (e.g. O'Brien & Parker 1994; Chambodut *et al.*

2005) have concluded that local lithospheric features may not be well represented by an SH representation since the corresponding model parameters are global basis functions that depend on the entire data set and its associated noise. When modelling the lithospheric magnetic field, local basis functions may arguably be more suitable, for instance (depleted) harmonic splines (Langel & Whaler 1996), wavelet functions (Maisinger *et al.* 2004; Mayer & Maier 2006), spherical triangle tessellations (Stockmann *et al.* 2009) and equivalent dipole sources (e.g. Covington 1993; Langlais *et al.* 2004). Another possibility is to use spectral, but domain-limited basis functions, for example spherical caps (Haines 1985; Thébault 2006, 2008) or spherical Slepians (Beggan *et al.* 2013). The current study builds on the method introduced by O'Brien & Parker (1994), applying equivalent monopole sources to represent the lithospheric field. Advantages of this method include its ease of application to data from various altitudes, the possibility to carry out both global and local modelling, as well as the ease of transformation into a spherical harmonic form (see Section 2.2). The latter is extremely useful for comparisons to state-of-the-art spherical harmonic

models of the global lithospheric field such as the MF7 serial model (Maus *et al.* 2008; Maus 2010), the CHAOS-4 model (Olsen *et al.* 2014) and CM5 (Sabaka *et al.* 2015), the latest version in the Comprehensive Model series. The use of local basis functions has the further advantage that when data noise is concentrated in specific regions (e.g. the polar regions), only model parameters in the vicinity are affected, while all model parameters are adversely affected if global basis functions such as spherical harmonics are used.

In Section 2, we present our formulation of the equivalent source method. The technique is then applied to a test case involving CHAMP data from January 2009 to September 2010. CHAMP data are currently the basis for the best available model of the lithospheric field (Maus *et al.* 2008; Maus 2010; Lesur *et al.* 2013; Sabaka *et al.* 2015). The CHAMP data and their processing are described in Section 3. Our model estimation procedure, involving iteratively reweighted least-squares (IRLS; Constable 1988; Olsen 2002) is described in Section 4. The approach involves over-parameterizing the number of monopoles and applying model regularization to control the model complexity. Following Stockmann *et al.* (2009), we test both conventional quadratic regularization (QR) and maximum entropy regularization (ER) techniques (Gull & Skilling 1999; Jackson *et al.* 2007). The former derives models of minimal source amplitudes, while the maximum entropy regularization models are characterized by minimal complexity for a given misfit to the observations. Results and their discussion are presented in Section 5 and we conclude in Section 6 with some perspectives regarding future applications of the method.

2 MODELLING TECHNIQUE

We describe the geomagnetic field in a geocentric reference frame by the spherical coordinates $\mathbf{r} = (r, \theta, \phi)$, where r denotes the radial distance from the centre of the Earth, θ denotes the geocentric co-latitude and ϕ denotes the eastern longitude. Currents in the ionosphere are neglected and the quasi-stationary approximation is adopted, such that the magnetic vector field \mathbf{B} above the Earth's surface is described by a scalar potential $\mathbf{B} = -\nabla\Phi(r, \theta, \phi)$ where $\nabla^2\Phi(r, \theta, \phi) = 0$. The solution of Laplace's equation can then be written as a spherical harmonic expansion. The corresponding solution for internal geomagnetic sources is usually expressed as

$$\Phi(\mathbf{r}) = a \sum_{n=0}^{\infty} \left(\frac{a}{r}\right)^{n+1} \sum_{m=0}^n [g_n^m \cos(m\phi) + h_n^m \sin(m\phi)] P_n^m(\cos\theta), \quad (1)$$

where $a = 6371.2$ km is the reference radius given by the mean radius of the Earth, $P_n^m(\cos\theta)$ are the Schmidt semi-normalized associated Legendre functions and $[g_n^m, h_n^m]$ are the time-dependent Gauss coefficients of order m and degree n (Blakely 1996).

In this study, we have removed estimates of the core field and large-scale magnetospheric sources derived from the CHAOS-4 model from the magnetic field observations, hence we are only concerned with the static lithospheric field component.

2.1 Equivalent source formulation

Having N measurement locations $\mathbf{r}_i = [r_i, \theta_i, \phi_i]$ (for $i = 1, \dots, N$), the magnetic scalar potential can be modelled as a linear combination of K globally distributed equivalent potential field sources (monopoles) located at $\mathbf{s}_k = [r_k, \theta_k, \phi_k]$ and with source strength q_k (for $k = 1, \dots, K$) measured in nT. Following O'Brien & Parker

(1994) and Blakely (1996), the corresponding potential can be expressed as

$$\begin{aligned} \hat{\Phi}(\mathbf{r}_i) &= \sum_{k=1}^K q_k \frac{r_k^2}{r_{ik}} \\ &= \sum_{k=1}^K r_k q_k \sum_{n=0}^{\infty} \left(\frac{r_k}{r_i}\right)^{n+1} P_n(\cos\mu_{ik}), \quad \text{with } K < N \quad (2) \end{aligned}$$

where $r_{ik} = |\mathbf{r}_i - \mathbf{s}_k|$ and μ_{ik} are the distance and angle between the position vectors of measurement i and source k , respectively,

$$\begin{aligned} r_{ik} &= \sqrt{r_i^2 + r_k^2 - 2r_i r_k \cos(\mu_{ik})} \\ \cos(\mu_{ik}) &= \cos(\theta_i) \cos(\theta_k) + \sin(\theta_i) \sin(\theta_k) \cos(\phi_i - \phi_k). \quad (3) \end{aligned}$$

Applying the decomposition formula for $P_n(\cos\mu_{ik})$ to eq. (2) (Torge 2001) and employing Schmidt-semi-normalization of the surface spherical harmonics (Blakely 1996), the potential due to monopole sources is

$$\begin{aligned} \Phi(\mathbf{r}_i) &= \sum_{k=1}^K r_k q_k \sum_{n=0}^{\infty} \left(\frac{r_k}{r_i}\right)^{n+1} \\ &\quad \times \sum_{m=0}^n P_n^m(\cos\theta_i) P_n^m(\cos\theta_k) \cos(m\phi_i - m\phi_k). \quad (4) \end{aligned}$$

Comparing the spherical harmonic and equivalent source potential expansion (eqs 1 and 4, respectively) enables the conventional spherical harmonic Gauss coefficients to be obtained directly from the equivalent source coefficients q_k ,

$$g_n^m = \sum_{k=1}^K \left(\frac{r_k}{a}\right)^{n+2} q_k P_n^m(\cos\theta_k) \cos(m\phi_k) \quad (5)$$

$$h_n^m = \sum_{k=1}^K \left(\frac{r_k}{a}\right)^{n+2} q_k P_n^m(\cos\theta_k) \sin(m\phi_k). \quad (6)$$

Note that eqs (5) and (6) provide a means of estimating a local power spectrum by considering the monopoles only within a region of interest, implicitly assuming those elsewhere are zero and renormalizing the power spectra accounting only for the area considered.

The Mauersberger–Lowes spherical harmonic power spectrum $R(n)$ due to internal sources, which is the squared magnitude of the magnetic field averaged over a spherical surface of radius r , is given by (Lowes 1974)

$$R(n) = (n+1) \left(\frac{a}{r}\right)^{(2n+4)} \sum_{m=0}^n [(g_n^m)^2 + (h_n^m)^2]. \quad (7)$$

All power spectrum illustrations below are given for $r = a$.

The comparison of two different lithospheric field models, with different sets of Gauss coefficients, $[g_n^m, h_n^m]$ and $[g_n^{\prime m}, h_n^{\prime m}]$, respectively, can be visualized using the degree correlation (Langel (1998), eq. 4.23)

$$\rho(n) = \frac{\sum_{m=0}^n (g_n^m g_n^{\prime m} + h_n^m h_n^{\prime m})}{\sqrt{\sum_{m=0}^n [(g_n^m)^2 + (h_n^m)^2] \sum_{m=0}^n [(g_n^{\prime m})^2 + (h_n^{\prime m})^2]}}. \quad (8)$$

Whenever $\rho \geq 0.7$, models are usually considered to be well correlated (Arkani-Hamed *et al.* 1994; Sabaka & Olsen 2006). Compared to the power spectra representation, degree correlations give no information on the magnetic field magnitudes but rather on the respective phase differences (Olsen *et al.* 2006).

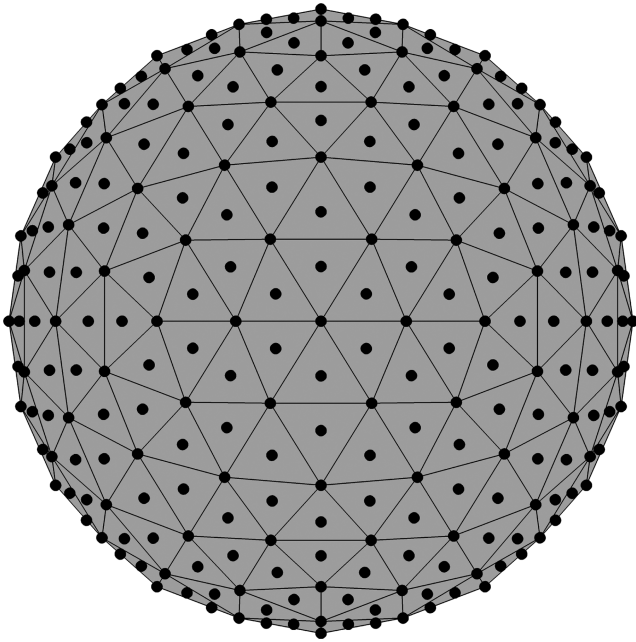


Figure 1. Icosahedron grid with refinement level $L = 2$. The corresponding sources are placed at the vertices and triangle midpoints. This study applies $L = 5$ corresponding to 30 722 source locations.

Another way of illustrating the model differences is by looking at the relative difference between each coefficient in a degree versus order matrix, $\underline{\underline{S}}$. For the difference between g_n^m and $g_n^{\prime m}$ we have

$$S(n, m) = 100 \cdot \frac{g_n^m - g_n^{\prime m}}{\sqrt{\frac{1}{(2n+1)} \sum_{m=0}^n \left[(g_n^{\prime m})^2 + (h_n^{\prime m})^2 \right]}}, \quad (9)$$

and similarly for the corresponding h_n^m coefficients. The coefficient differences are normalized with respect to the mean spectral amplitude of a reference model, with $[g_n^{\prime m}, h_n^{\prime m}]$ being the corresponding Gauss coefficients (Olsen *et al.* 2005, eq. 5.3). Note that the factor 100 in eq. (9) indicates that the normalized coefficient differences are given in per cent.

We have chosen to use magnetic monopoles as equivalent sources due to their simplicity and mathematical convenience. Like dipoles, they are a solution to Laplace's equation and produce a potential field (e.g. Toyoshima *et al.* 2008). However, according to Maxwell's equations we have $\nabla \cdot \mathbf{B} = 0$, which means that individual monopoles do not exist. Here we use monopoles only as a mathematical tool for representing the lithospheric magnetic field models and impose an additional constraint (see Section 4.5) to ensure that the divergence-free constraint is satisfied.

2.2 Distribution of sources

In this study, we apply an icosahedral grid (Baumgardner & Fredrickson 1985) with monopoles placed at both vertices and triangle midpoints. The corresponding grid size is defined by the source depth and grid refinement level L . A grid of refinement level $L = 0$ consists of 20 identical equilateral triangular faces and 12 vertices on a unit sphere. Each vertex is thereby surrounded by either five or six faces. Increasing the refinement level by 1, every face is further subdivided into four triangles, see Fig. 1. In this study, we use $L = 5$, consisting of $K = 30\,722$ locations at the vertices and midpoints, all projected on a sphere of radius $a - 100$ km so the distance between the satellite data and the monopoles is greater than

Table 1. Median angular distance and arc length between two adjacent sources for different icosahedron grid refinement levels L . The arc length is given at the Earth's surface. Both vertices and midpoints are taken into account in K .

L	K	Angular distance (deg)	Arc length (km)
3	1922	3.52	391
4	7683	1.75	195
5	30722	0.98	109
6	122882	0.49	54
7	491522	0.24	27

the separation between the monopoles. We have chosen to include the centre points as a means of grid refinement without resorting to a higher refinement level, which would result in a large increase in the number of sources and hence the calculation time.

Table 1 lists the median angular separation between two adjacent sources for different grid refinement levels. The values are calculated from the average distance between sources and their five nearest neighbours. The applied grid refinement level corresponds to a median grid spacing of 0.98° , equivalent to an arc length of 109 km at the Earth's surface. Synthetic tests demonstrated that for the regularized models presented here, the surface field results were not affected by the equivalent source locations.

The chosen source depth of $a - 100$ km is based on a synthetic test where the magnetic field signatures at Earth's surface produced by monopoles with a horizontal spacing of 1° (very close to the applied angular distance of 0.98°) were found to be negligible.

3 DATA, PRE-PROCESSING AND ERROR BUDGET

CHAMP 30 s three-component vector field data between 2009 January 1 and 2010 September 2 are used in this study. During that period the satellite was at its lowest altitude (below 300 km) and solar activity was also rather quiet, making the data particularly suitable for lithospheric magnetic field studies. Estimates of core and large-scale magnetospheric sources are removed from the measurements using the geomagnetic field model CHAOS-4, and we use the same data selection as employed in CHAOS-4 (Olsen *et al.* 2006, 2014). Important to mention here are the quiet-time conditions (Kp-index $\leq 2^0$ for quasi-dipole (QD) latitudes equatorward of $\pm 55^\circ$ and the merging electric field at the magnetopause $E_m \leq 0.8$ mV m $^{-1}$ for QD latitudes poleward of $\pm 55^\circ$) and dark region data (sun at least 10° below the horizon) selection criteria, which aim to minimize the influence of the ionospheric field. Further, the contribution from disturbances of the magnetospheric ring current is minimized by only selecting data with hourly RC-index variations smaller than 2 nT hr $^{-1}$ (Olsen *et al.* 2014).

Our implementation of IRLS assumes independent and Huber distributed (i.e. Gaussian distributed in the centre, Laplacian distributed in the tails) residuals. We additionally remove gross outliers with absolute residual values > 100 nT from the data set in an effort to avoid mapping strongly correlated noise from badly disturbed tracks into the lithospheric magnetic field models.

Regarding the data error budget, we implement data uncertainties depending on the QD latitude (Richmond 1995; Emmert *et al.* 2010) independently for the three vector field components, B_r , B_θ and B_ϕ , as shown in Fig. 2. The uncertainties (standard deviations) σ_p (where $p = r, \theta$ or ϕ) are derived using the robust algorithm of Driessen & Rombouts (2007) applied to residuals (obtained by subtracting from the data predictions from the CHAOS-4 model,

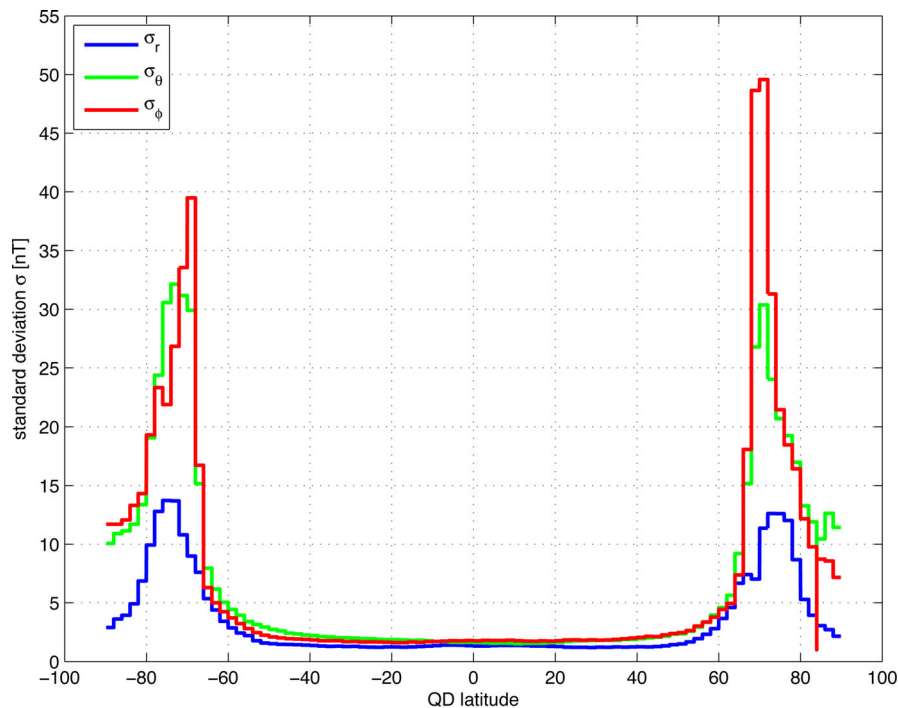


Figure 2. Latitude-dependent standard deviation values σ_p (where $p = r, \theta$ or ϕ). Values are derived for each QD latitude band of 2° (the Northern Hemisphere is indicated by positive QD latitude values) using the robust procedure of Driessen & Rombouts (2007).

including its core, crustal and external parts) in 2° latitudinal bands. The QD coordinate system is suitable for describing processes due to unmodelled ionospheric sources, which we assume dominate the residuals, especially at polar latitudes.

The CHAMP satellite tracks are defined by a near polar orbit with an inclination of 87.3° . Thus, there are no data within 2.7° of the poles, which introduces instabilities in the determination of high degree spherical harmonic zonal coefficients. In order to counteract this ‘polar gap’ effect, 12 257 synthetic (noise-free) values of the radial field component are added in the polar regions between $\pm 0.5^\circ$ and 4° at 300 km altitude derived from the CHAOS-4I model up to SH degree $n = 60$. The synthetic data represent 2.89 per cent of the total data set. Except for the polar gap regions, we use all three measurement components in the model derivation. We have also carried out tests without adding synthetic data in the polar gap and find very similar results at non-polar gap locations, see Section 5. This illustrates one advantage of the local nature of our equivalent source method.

4 MODEL ESTIMATION

In this section, we describe our scheme for estimating equivalent source models of the lithospheric field from satellite data. Based on a regularized IRLS approach, the scheme involves iteratively minimizing a penalty function measuring both the misfit to the observations and also the complexity of the model.

In Section 4.1, we present our mathematical formulation of the inverse problem. The IRLS numerical scheme used to obtain solutions is set out in Section 4.2. Section 4.3 gives the details in the case that model complexity is measured using a traditional quadratic norm, and Section 4.4 gives the corresponding details when an entropy-based measure of model complexity is instead employed. The method of enforcing the divergence-free condition, a necessary feature of any scheme based on monopoles, is described in Section 4.5. The diagnostic measures of model resolution we em-

ploy are given in Section 4.6, and finally a short summary of our lithospheric field model estimation scheme is given in Section 4.7.

4.1 Formulation of the inverse problem

The magnetic field \mathbf{B} due to the equivalent monopole sources measured at a given location i is calculated using the negative gradient of eq. (2),

$$\begin{aligned} \mathbf{B}(\mathbf{r}_i) &= -\nabla \hat{\Phi}(\mathbf{r}_i) \\ &= -\sum_{k=1}^K q_k \nabla \frac{r_k^2}{r_{ik}}. \end{aligned} \quad (10)$$

The data for a particular field component p , where p can be r, θ , or ϕ , is the projection of \mathbf{B} onto the direction given by the unit vector $\hat{\mathbf{e}}_p$,

$$\begin{aligned} B_{i,p} &= -\sum_{k=1}^K q_k \left[\hat{\mathbf{e}}_{i,p} \cdot \nabla_p \frac{r_k^2}{r_{ik}} \right] \\ &= \sum_{k=1}^K q_k g_{ik,p}, \end{aligned} \quad (11)$$

where $g_{ik,p}$ are the individual elements of the Green’s matrix representing the directional derivatives of the k th source evaluated in the direction p and at the location \mathbf{r}_i .¹ The corresponding full expressions are given in the Appendix.

¹The Green’s matrix elements for equivalent sources are derived in O’Brien & Parker (1994). However, it appears that the corresponding eqs (C2) and (C3) contain a typographical error. In formula (C3) we have changed the signs in front of rs to be negative. In eq. (C2), the formulae for $B_\theta(\mathbf{r})$ and $B_\phi(\mathbf{r})$ have been multiplied by -2 and 2 , respectively. In the formula of $B_r(\mathbf{r})$, the factor 2 was removed both in the numerator and denominator.

Applying the above scheme to all measurements, the forward problem described by eq. (11) may be written as

$$\mathbf{B} = \underline{\underline{\mathbf{G}}}\mathbf{q} \quad (12)$$

where $\mathbf{B} = [\mathbf{B}_r, \mathbf{B}_\theta, \mathbf{B}_\phi]$ is a column vector containing model predictions for all $3N$ vector components at the N locations of magnetic field measurements, $\underline{\underline{\mathbf{G}}} = [\underline{\underline{\mathbf{G}}}_r, \underline{\underline{\mathbf{G}}}_\theta, \underline{\underline{\mathbf{G}}}_\phi]$ represents the corresponding $3N \times K$ Green's matrix and \mathbf{q} is the model vector of all K source strengths q_k .

The inverse problem then consists of finding a model \mathbf{q} that minimizes the error vector \mathbf{e} between the observed data \mathbf{d} and the model predictions \mathbf{B} ,

$$\begin{aligned} \mathbf{d} &= \mathbf{B} + \mathbf{e} \\ &= \underline{\underline{\mathbf{G}}}\mathbf{q} + \mathbf{e} \end{aligned} \quad (13)$$

4.2 Regularized IRLS solution

Determination of the lithospheric field at Earth's surface from noisy data collected at satellite altitude is an ill-posed and non-unique inverse problem. We find solutions to this problem using an IRLS algorithm (e.g. Walker & Jackson 2000) including model regularization. This involves minimizing both the differences between model predictions and measurements (a misfit norm) and also a measure of the model complexity \mathbf{R} (regularization norm). The objective function Θ we minimize is of the form

$$\Theta(\mathbf{q}) = (\mathbf{d} - \underline{\underline{\mathbf{G}}}\mathbf{q})^T \underline{\underline{\mathbf{W}}}(\mathbf{d} - \underline{\underline{\mathbf{G}}}\mathbf{q}) + \lambda \mathbf{R}(\mathbf{q}) \quad (14)$$

where

$$\underline{\underline{\mathbf{W}}} = \underline{\underline{\mathbf{C}}}^{-1/2} \underline{\underline{\mathbf{H}}}\underline{\underline{\mathbf{C}}}^{-1/2}. \quad (15)$$

The data weight matrix $\underline{\underline{\mathbf{W}}}$ consists of two parts: (i) a diagonal inverse data error covariance matrix $\underline{\underline{\mathbf{C}}}^{-1} = \frac{\sin\theta}{\sigma^2}$ that accounts for the expected data error variances σ^2 (see Section 3) and provides equal area weighting; (ii) a Huber weighting matrix $\underline{\underline{\mathbf{H}}}$ that depends on the residuals between the model predictions and the observations (e.g. Constable 1988). The regularization parameter λ (nT^{-2}) quantifies the trade-off between the misfit and regularization norm (e.g. Menke 2012). Large λ values result in models of low complexity but with large residuals, while the opposite is the case for small λ values.

A Newton-type iterative scheme is used to minimize the objective function of eq. (14), such that the model prediction at the $j + 1$ iteration is given by

$$\begin{aligned} \mathbf{q}_{j+1} &= (2\underline{\underline{\mathbf{G}}}^T \underline{\underline{\mathbf{W}}}\underline{\underline{\mathbf{G}}} + \lambda \nabla \nabla \mathbf{R}(\mathbf{q}_j))^{-1} \\ &\quad \times (2\underline{\underline{\mathbf{G}}}^T \underline{\underline{\mathbf{W}}}\mathbf{d} + \lambda \nabla \nabla \mathbf{R}(\mathbf{q}_j)\mathbf{q}_j - \lambda \nabla \mathbf{R}(\mathbf{q}_j)). \end{aligned} \quad (16)$$

A new solution is thus derived from the model \mathbf{q}_j and the Huber weights $\underline{\underline{\mathbf{H}}}_j$ (that appear in $\underline{\underline{\mathbf{W}}}_j$) from the previous iteration. We iterate eq. (16) until the convergence criterion $\|\mathbf{q}_j - \mathbf{q}_{j+1}\|/\|\mathbf{q}_{j+1}\| < 0.01$ is met.

The Huber weights in the diagonal matrix $\underline{\underline{\mathbf{H}}}_j = [\mathbf{h}_{r,j}, \mathbf{h}_{\theta,j}, \mathbf{h}_{\phi,j}]$ (e.g. Huber 1964; Constable 1988) are obtained from the residuals $\mathbf{e}_{p,j}$ from the j th iteration, with $p = r, \theta$ or ϕ , normalized by the expected latitude-dependent standard deviation values σ_p from Fig. 2. Considering the i th vector field observation, the Huber weight for a given component p is

$$h_{p,j}(i) = \begin{cases} 1 & \text{if } \epsilon_{p,j}(i) \leq 1.5, \\ 1.5/\epsilon_{p,j}(i) & \text{if } \epsilon_{p,j}(i) > 1.5 \end{cases} \quad (17)$$

where

$$\epsilon_{p,j} = |\mathbf{e}_{p,j}/\sigma_p|. \quad (18)$$

This results in residuals much larger than expected being down-weighted in the least-squares scheme. The changes in $\epsilon_{p,j}$ with iteration j are due to changes in the model misfit $\mathbf{e}_{p,j}$, and not to changes in σ_p .

4.3 Quadratic regularization

We consider a very simple form of quadratic regularization, defined by the Euclidean length of the model solution, $\mathbf{R}^{\text{QR}}(\mathbf{q}) = \mathbf{q}^T \mathbf{q}$. Minimizing the objective function with respect to \mathbf{q} then results in the following simplified version of eq. (16)

$$\mathbf{q}_{j+1}^{\text{QR}} = (\underline{\underline{\mathbf{G}}}^T \underline{\underline{\mathbf{W}}}\underline{\underline{\mathbf{G}}} + \lambda \mathbf{I})^{-1} \underline{\underline{\mathbf{G}}}^T \underline{\underline{\mathbf{W}}}\mathbf{d}. \quad (19)$$

The corresponding solution has the smallest possible sum of squares of the monopole values, for a chosen level of misfit. This criterion, however, may not always be geologically useful, in particular because there are several very large amplitude local magnetic field anomalies, for example, the West African Craton anomaly and the Bangui anomaly. Allowing a model to possess high amplitude local anomalies, while at the same time retaining a simple morphology, is possible by regularizing the model entropy rather than its squared amplitude. This is the subject of the next section. The investigated quadratic regularization models, with their different λ values, share the same starting point, a well-converged, but unregularized ($\lambda = 0$), solution.

4.4 Maximum entropy regularization

In order to account for the large amplitudes of local lithospheric field anomalies, we investigate the effect of regularizing the model information complexity rather than its amplitude. The entropy regularization method applied here was previously described in detail by Jackson *et al.* (2007) and Stockmann *et al.* (2009). We note that maximum entropy regularization is naturally implemented in the physical domain, rather than in spectral model space; it can therefore be very easily implemented by considering the entropy of different arrangements of the equivalent sources.

Gull & Skilling (1999) define the entropy S of a model \mathbf{q} , which can consist of both negative and positive values, as

$$S(\mathbf{q}, \omega) = \sum_{k=1}^K \left[\psi_k - 2\omega - q_k \ln \left(\frac{\psi_k + q_k}{2\omega} \right) \right]. \quad (20)$$

We work with the related negative entropy (negentropy) regularization norm (Gillet *et al.* 2007)

$$\mathbf{R}^{\text{ER}}(\mathbf{q}, \omega) = -4\omega S(\mathbf{q}, \omega) \quad (21)$$

with ω being a default parameter which defines the scale of the entropy function (Maisinger *et al.* 2004) and $\psi_k = \sqrt{q_k^2 + 4\omega^2}$. The negentropy \mathbf{R}^{ER} becomes identical to the quadratic norm for large values of ω , thus making comparisons between the two regularization methods possible. Using $\mathbf{R}^{\text{ER}}(\mathbf{q}, \omega)$ as the regularization norm, eq. (16) becomes

$$\mathbf{q}_{j+1}^{\text{ER}} = (2\underline{\underline{\mathbf{G}}}^T \underline{\underline{\mathbf{W}}}\underline{\underline{\mathbf{G}}} + \lambda \alpha_j)^{-1} \left(2\underline{\underline{\mathbf{G}}}^T \underline{\underline{\mathbf{W}}}\mathbf{d} + \lambda \alpha_j \mathbf{q}_j^{\text{ER}} - 4\lambda \omega \beta_j \right) \quad (22)$$

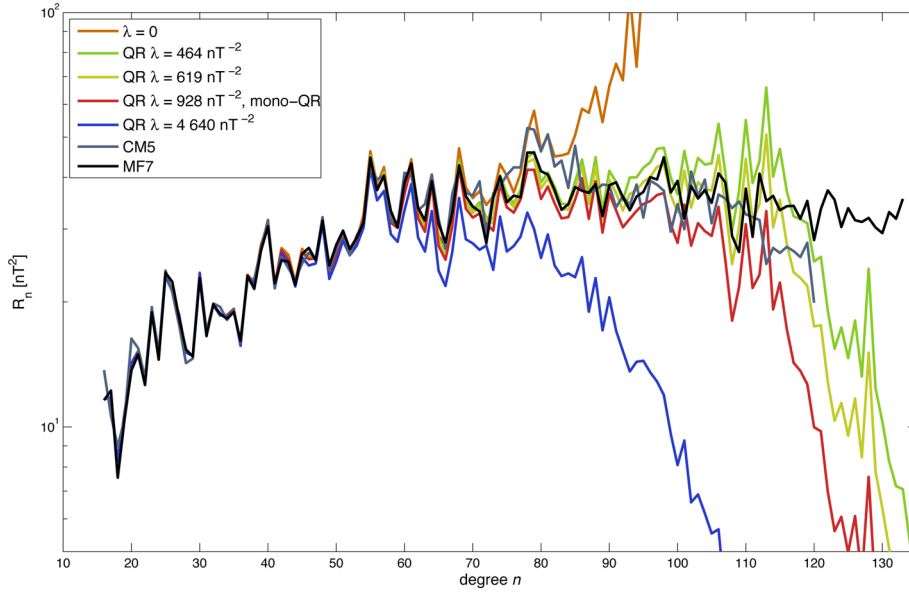


Figure 3. Power spectra for the investigated quadratically regularized (QR) models with different regularization parameters λ , compared to some recent lithospheric field models (CM5: Sabaka *et al.* (2015) and MF7: Maus *et al.* (2008); Maus (2010)). The model with $\lambda = 928 \text{ nT}^{-2}$, represented by the red line, is chosen as our preferred model mono-QR. The corresponding lithospheric radial magnetic field at the Earth's surface is illustrated in the upper part of Fig. 4.

with

$$\alpha_j = \text{diag} \left(\frac{4\omega}{\psi_{1,j}}, \frac{4\omega}{\psi_{2,j}}, \dots, \frac{4\omega}{\psi_{K,j}} \right)$$

$$\beta_j = \left(\ln \left(\frac{\psi_{1,j} + q_{1,j}}{2\omega} \right), \ln \left(\frac{\psi_{2,j} + q_{2,j}}{2\omega} \right), \dots, \ln \left(\frac{\psi_{K,j} + q_{K,j}}{2\omega} \right) \right). \quad (23)$$

Converged quadratic regularization models with the same λ were used as the starting conditions for the investigated maximum entropy models.

4.5 Enforcing the divergence-free condition

Since isolated magnetic monopoles do not exist ($\nabla \cdot \mathbf{B} = 0$), we must also enforce an additional condition that ensures zero net magnetic flux (O'Brien & Parker 1994)

$$\sum_{k=1}^K q_k = 0. \quad (24)$$

This requirement can be implemented using a Lagrangian method by applying the following scheme (Sabaka, private communication, 2011):

$$\mathbf{q}_{j+1}^c = \mathbf{q}^* - \mathbf{A}\mathbf{L}(\mathbf{L}^T \mathbf{q}^*)(\mathbf{L}^T \mathbf{A}\mathbf{L})^{-1}$$

$$\mathbf{A} = (\underline{\mathbf{G}}^T \underline{\mathbf{W}}_j \underline{\mathbf{G}} + \lambda \mathbf{I})^{-1}, \quad (25)$$

where \mathbf{L} is a $1 \times K$ unity row vector and \mathbf{q}^* now represents either a quadratic ($\mathbf{q}_{j+1}^{\text{QR}}$) or maximum entropy ($\mathbf{q}_{j+1}^{\text{ER}}$) unconstrained model solution from eqs (19) and (22).

4.6 Model resolution and number of degrees of freedom

An important method of quantitatively assessing inversion results is to compute the model resolution matrix $\underline{\mathcal{R}}$. This represents the

mapping between the estimated and true model parameters. For a quadratic regularization, $\underline{\mathcal{R}}$ takes the form (e.g. Bloxham *et al.* 1989; Menke 2012)

$$\underline{\mathcal{R}}^{\text{QR}} = (\underline{\mathbf{G}}^T \underline{\mathbf{W}} \underline{\mathbf{G}} + \lambda \mathbf{I})^{-1} \underline{\mathbf{G}}^T \underline{\mathbf{W}} \underline{\mathbf{G}}. \quad (26)$$

The corresponding linearized approximation for the maximum entropy approach is

$$\underline{\mathcal{R}}^{\text{ER}} = (2\underline{\mathbf{G}}^T \underline{\mathbf{W}} \underline{\mathbf{G}} + \lambda \alpha)^{-1} 2\underline{\mathbf{G}}^T \underline{\mathbf{W}} \underline{\mathbf{G}}. \quad (27)$$

A comparison and assessment of the achieved resolution of two regularized models can thereby be performed. In particular, the effective number of degrees of freedom may be obtained from the trace of the respective resolution matrices.

4.7 Summary of model estimation scheme

For convenient reference, we summarize here our model estimation scheme:

(i) Inputs:

\mathbf{d} : the observed vector field magnetic data.

σ_p : *a priori* standard deviations for the data errors (latitude-dependent for each field component).

λ : the regularization parameter, and ω the entropy default parameter for ER models.

$\underline{\mathbf{G}}$: the Green's matrix connecting the data to the model parameters.

(ii) Initial conditions

Unregularized model ($\lambda = 0$): starts from unity Huber weights and model values \mathbf{q} all set to zero.

QR models: start from converged $\lambda = 0$ model and corresponding Huber weights.

ER models: start from converged QR model with same λ and corresponding Huber weights.

(iii) Iteration step: model \mathbf{q}_{j+1} from model \mathbf{q}_j and its associated Huber weights

Unregularized model: iterate eq. (19) with $\lambda = 0$.

QR models: iterate eq. (19), with given and fixed λ .

ER models: iterate eq. (22), with given and fixed λ and ω .

Table 2. Normalized (by latitude-dependent standard deviation values) and un-normalized Huber-weighted RMS model residual values between the CHAMP observations and the models MF7 ($n_{\max} = 133$), CM5 ($n_{\max} = 120$), CHAOS-4 ($n_{\max} = 100$), and a selection of QR models and ER models at satellite altitude. The results for models mono-QR and mono-ER are highlighted in bold. Here we define $\Delta B = \sqrt{\Delta B_r^2 + \Delta B_\theta^2 + \Delta B_\phi^2}$. The suffixes ‘polar’ and ‘non-polar’ represent data of absolute QD latitudes $>55^\circ$ and $<55^\circ$, respectively.

	MF7	CM5	CHAOS-4	QR models				ER models	
$\lambda(nT^{-2}) =$	–	–	–	4640	928	619	464	928	4640
$\omega(nT) =$	–	–	–	–	–	–	–	55×10^{-4}	25×10^{-4}
Normalized									
RMS ΔB_r (–)	1.31	1.34	1.30	1.29	1.29	1.29	1.29	1.29	1.29
RMS ΔB_r polar (–)	1.43	1.45	1.43	1.43	1.43	1.43	1.43	1.43	1.43
RMS ΔB_r non-polar (–)	1.22	1.26	1.21	1.18	1.18	1.18	1.18	1.18	1.18
RMS ΔB_θ (–)	1.26	1.27	1.26	1.26	1.26	1.26	1.26	1.26	1.26
RMS ΔB_θ polar (–)	1.38	1.39	1.38	1.38	1.38	1.38	1.38	1.38	1.38
RMS ΔB_θ non-polar (–)	1.17	1.19	1.17	1.18	1.17	1.17	1.17	1.17	1.18
RMS ΔB_ϕ (–)	1.28	1.29	1.27	1.27	1.27	1.27	1.27	1.27	1.27
RMS ΔB_ϕ polar (–)	1.43	1.43	1.43	1.42	1.42	1.42	1.42	1.42	1.42
RMS ΔB_ϕ non-polar (–)	1.17	1.18	1.16	1.16	1.16	1.16	1.16	1.16	1.16
RMS ΔB (–)	1.28	1.30	1.28	1.27	1.27	1.27	1.27	1.27	1.27
RMS ΔB polar (–)	1.41	1.42	1.41	1.41	1.41	1.41	1.41	1.41	1.41
RMS ΔB non-polar (–)	1.19	1.21	1.18	1.17	1.17	1.17	1.17	1.17	1.17
Un-normalized									
RMS ΔB_r (nT)	7.41	7.44	7.39	7.41	7.40	7.40	7.40	7.40	7.41
RMS ΔB_r polar (nT)	11.43	11.44	11.41	11.45	11.44	11.44	11.44	11.44	11.45
RMS ΔB_r non-polar (nT)	1.66	1.71	1.64	1.61	1.61	1.60	1.60	1.60	1.61
RMS ΔB_θ (nT)	15.81	15.84	15.81	15.81	15.81	15.81	15.81	15.81	15.81
RMS ΔB_θ polar (nT)	24.52	24.56	24.52	24.51	24.51	24.51	24.51	24.51	24.51
RMS ΔB_θ non-polar (nT)	2.40	2.42	2.40	2.40	2.40	2.40	2.40	2.40	2.40
RMS ΔB_ϕ (nT)	17.29	17.29	17.28	17.26	17.25	17.25	17.25	17.25	17.26
RMS ΔB_ϕ polar (nT)	26.91	26.88	26.90	26.86	26.86	26.86	26.86	26.86	26.86
RMS ΔB_ϕ non-polar (nT)	2.25	2.27	2.23	2.23	2.23	2.23	2.23	2.23	2.23
RMS ΔB (nT)	14.19	14.21	14.18	14.17	14.17	14.17	14.17	14.17	14.17
RMS ΔB polar (nT)	22.05	22.06	22.04	22.02	22.02	22.02	22.02	22.02	22.02
RMS ΔB non-polar (nT)	2.13	2.16	2.12	2.11	2.11	2.11	2.11	2.11	2.11

Table 3. Similar to Table 2 but with statistics for only part of the African continent (area of the inserted plot in the left part of Fig. 10). The preferred models mono-QR and mono-ER are highlighted in bold. $\Delta B = \sqrt{\Delta B_r^2 + \Delta B_\theta^2 + \Delta B_\phi^2}$.

	MF7	CM5	CHAOS-4	QR models				ER models	
$\lambda(nT^{-2}) =$	–	–	–	4640	928	619	464	928	4640
$\omega(nT) =$	–	–	–	–	–	–	–	55×10^{-4}	25×10^{-4}
Normalized									
RMS ΔB_r (–)	4.05	4.29	4.07	1.20	1.20	1.20	1.20	1.20	1.20
RMS ΔB_θ (–)	2.10	2.21	2.11	1.11	1.11	1.11	1.11	1.11	1.11
RMS ΔB_ϕ (–)	2.52	2.57	2.47	1.15	1.15	1.15	1.15	1.15	1.15
RMS ΔB (–)	2.85	2.97	2.84	1.15	1.15	1.15	1.15	1.15	1.15
Un-normalized									
RMS ΔB_r (nT)	5.32	5.62	5.35	1.57	1.57	1.57	1.57	1.57	1.57
RMS ΔB_θ (nT)	3.76	3.95	3.79	2.01	2.01	2.01	2.01	2.01	2.01
RMS ΔB_ϕ (nT)	4.39	4.48	4.31	2.01	2.01	2.01	2.01	2.01	2.01
RMS ΔB (nT)	4.42	4.60	4.41	1.88	1.87	1.87	1.87	1.87	1.88

(iv) Implement divergence free condition via eq. (25)

(v) Test convergence criterion

$$\|\mathbf{q}_j - \mathbf{q}_{j+1}\| / \|\mathbf{q}_{j+1}\|$$

$$\times \begin{cases} > 0.01 & \text{return to (iii) and start next iteration,} \\ < 0.01 & \mathbf{q}_{j+1} \text{ is the converged model solution. END.} \end{cases}$$

5 RESULTS AND DISCUSSION

We begin this section by describing the results obtained using the QR approach. A wide range of regularization parameters were investigated, and a selection of models from the vicinity of the knee of the L-curve (Hansen 1998), with regularization parameters $\lambda = 4640$,

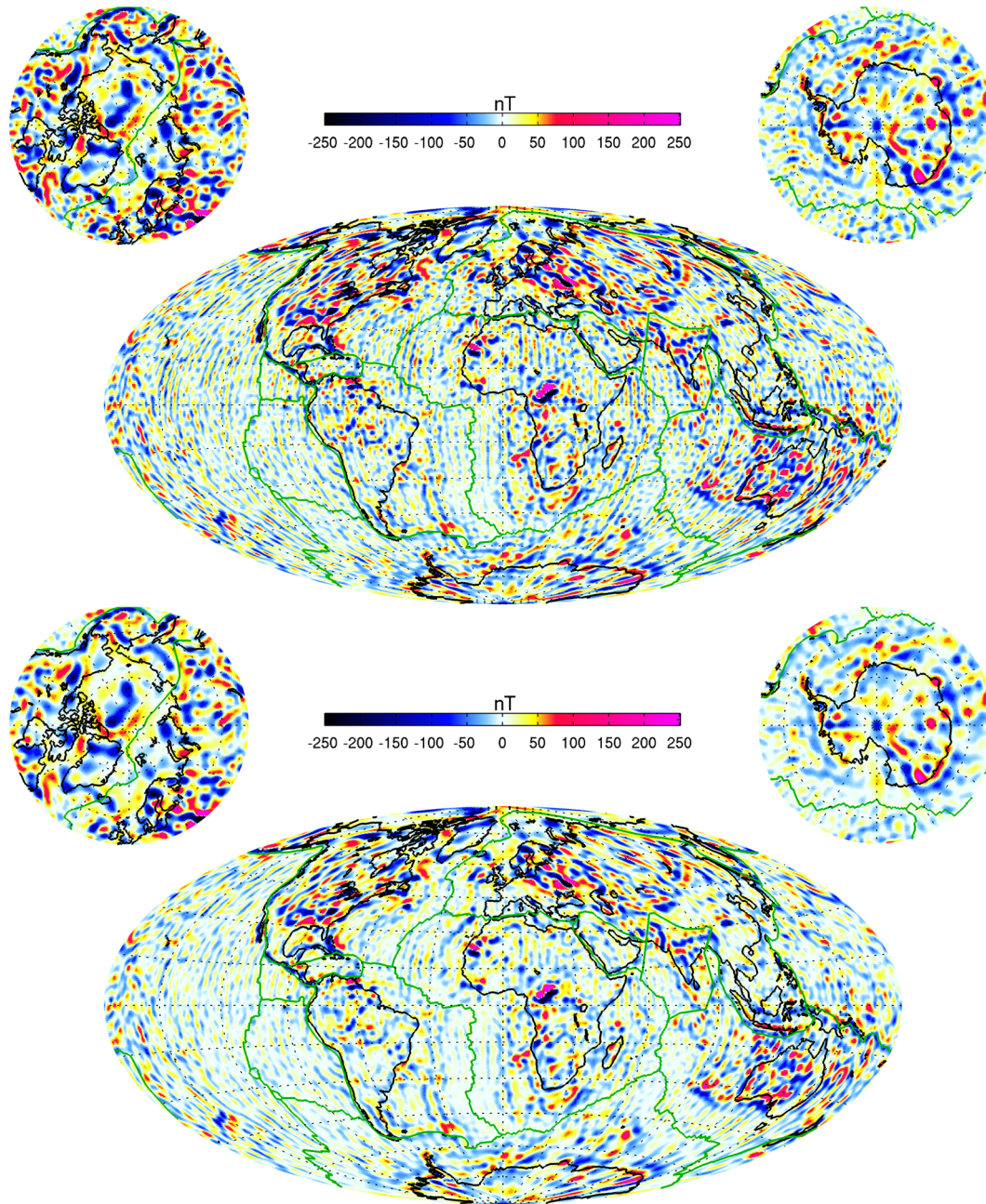


Figure 4. Top: lithospheric radial magnetic field corresponding to the preferred quadratic regularization model mono-QR with $\lambda = 928 \text{ nT}^{-2}$ at the Earth's surface. Bottom: similar figure for the preferred maximum entropy regularization model mono-ER with $\lambda = 4640 \text{ nT}^{-2}$ and $\omega = 25 \times 10^{-4} \text{ nT}$. The scale saturates at 250 nT. Note that both figures are the direct output of the corresponding monopole model rather than an approximation based on a truncated SH expansion. The corresponding model differences are illustrated in Fig. 8.

928, 619 and 464 nT^{-2} , were chosen for further analysis. All models were derived from the same unregularized ($\lambda = 0$) starting model, and they converged within five iterations. The model values \mathbf{q} were then converted into the spherical harmonic Gauss coefficients g_n^m and h_n^m using eqs (5) and (6). Fig. 3 illustrates the corresponding Mauersberger–Lowes power spectra, eq. (7), compared to the state-of-the-art lithospheric field models CM5 (Sabaka *et al.* 2015) and MF7 (Maus *et al.* 2008; Maus 2010). We observe the expected decrease in power at high spherical harmonic degrees with increasing regularization parameter.

An interesting question is whether our monopole models are more or less sensitive to the lack of data within the polar gap re-

gions, compared to SH field models which are known to be strongly affected by this problem above SH degree 60 (Olsen *et al.* 2014). We constructed models with and without synthetic data added in the polar gap regions. Both power spectra and global lithospheric field maps indicate that the monopole method is not dependent on having data in the polar gap regions. Differences in the field maps are only seen in the areas where synthetic data were added, while the power spectra are almost identical. The lack of sensitivity to the polar gap problem seems therefore to be an advantage of our models in comparison to models that are based on spherical harmonics.

Tables 2 and 3 present statistics comparing the fit of the models to selected CHAMP observations globally and locally (over

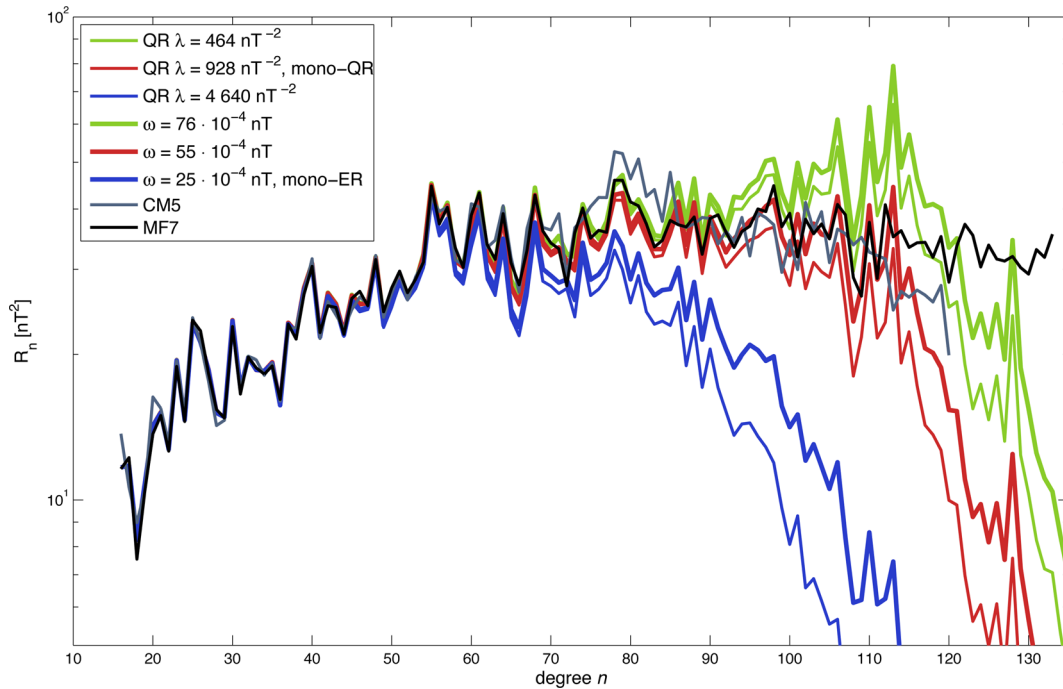


Figure 5. Power spectra for QR models (thin lines) and ER models (thick lines) compared to reference lithospheric field models. Models with the same regularization parameters are represented with the same colour.

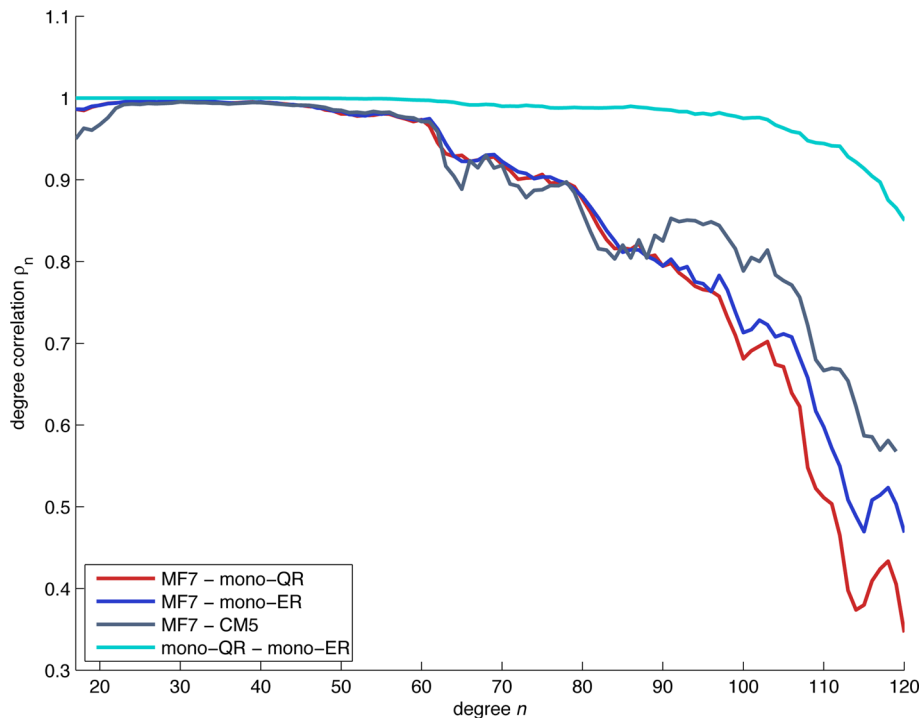


Figure 6. Degree correlation between MF7 and the spherical harmonic degrees of mono-QR, mono-ER and CM5. The monopole-based models reach a typical correlation limit of $\rho_n = 0.7$ (Arkani-Hamed *et al.* 1994; Sabaka & Olsen 2006) at SH degree $n = 100$. CM5 correlates well with MF7 up to SH degree $n = 108$. The light blue line shows the degree correlation between mono-QR and mono-ER.

part of the African continent), respectively. The corresponding model residual RMS values are given at satellite altitude and were derived using the weights implemented in the inversion. The upper half of the tables normalizes the values by dividing the residuals by the measurement error standard deviations of Fig. 2. As expected, the derived models in general fit the observations bet-

ter than both MF7 and CM5 with the various QR models having very similar residual values. However, looking at their respective global lithospheric radial magnetic field maps (not given here), we observe larger residuals especially in oceanic regions for decreasing regularization parameters. For example, in the Pacific and the North Atlantic ocean, north–south striping features appear which we

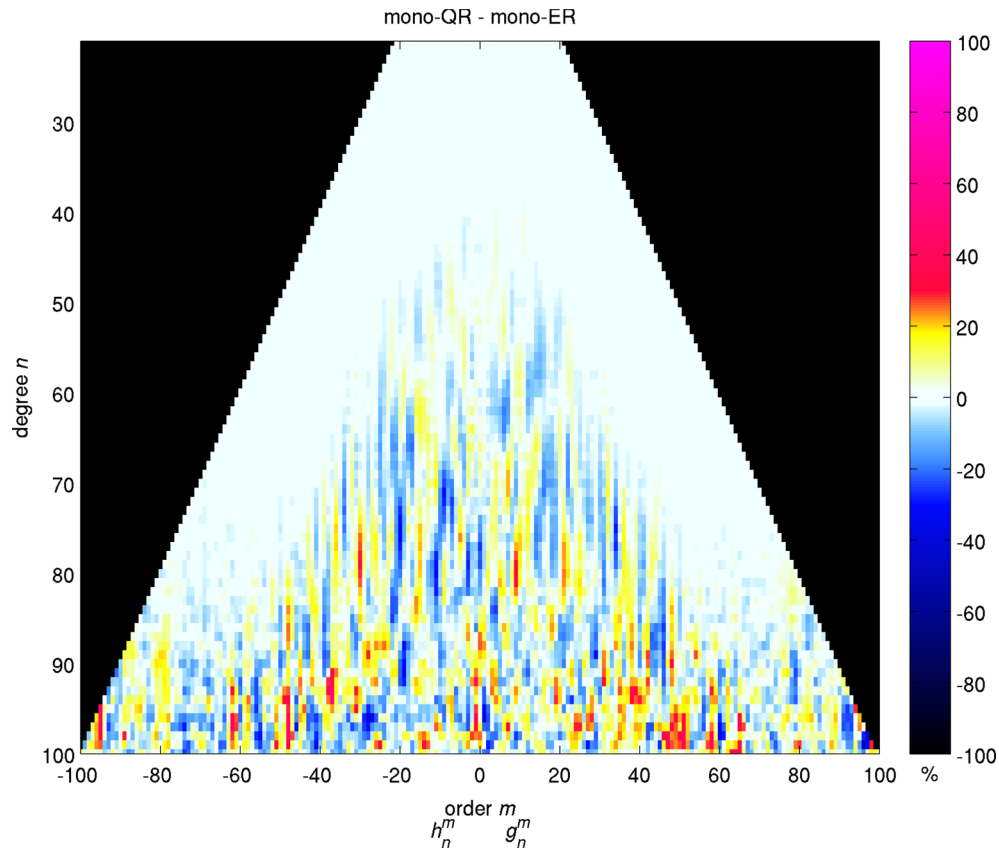


Figure 7. Normalized coefficient differences between mono-QR and mono-ER.

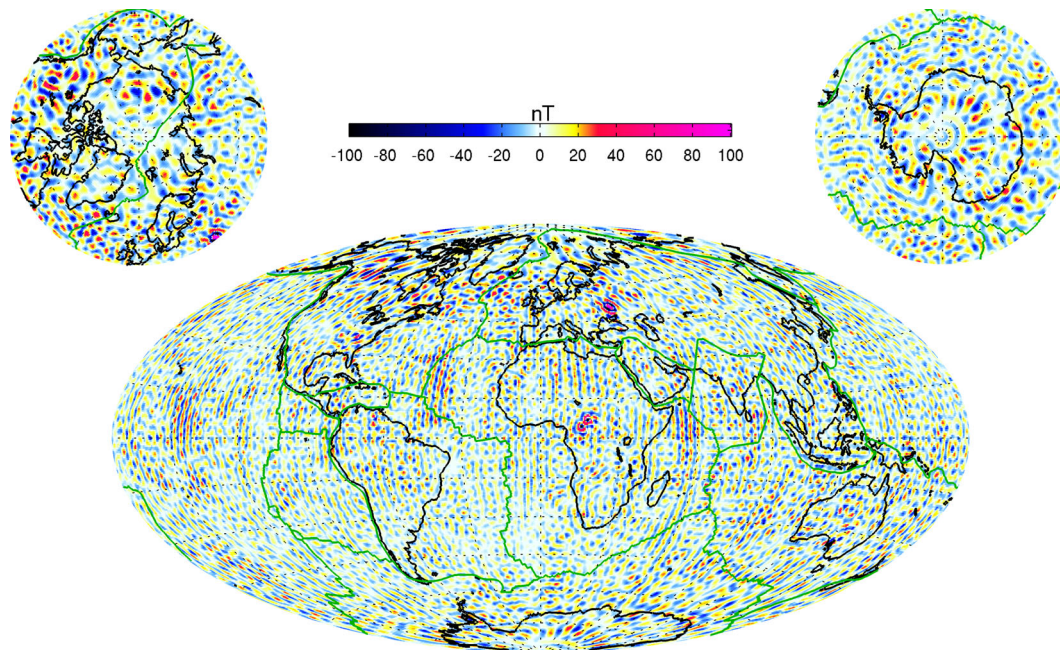


Figure 8. Lithospheric radial magnetic field difference between the quadratic regularization model mono-QR with $\lambda = 928 \text{ nT}^{-2}$ (5 iterations) and the maximum entropy regularization model mono-ER with $\lambda = 4640 \text{ nT}^{-2}$ and $\omega = 25 \times 10^{-4} \text{ nT}$ (10 iterations) at the Earth's surface. Note that the scale saturates at only 100 nT.

associate with unmodelled magnetospheric field signals still present in the data set. Taking the power spectra, statistical comparisons and radial field maps into account, we select the model with $\lambda = 928 \text{ nT}^{-2}$ to be the preferred

QR model of this study. Henceforth, we refer to this as model 'mono-QR'. The corresponding lithospheric radial magnetic field at the Earth's surface is presented in the upper part of Fig. 4.

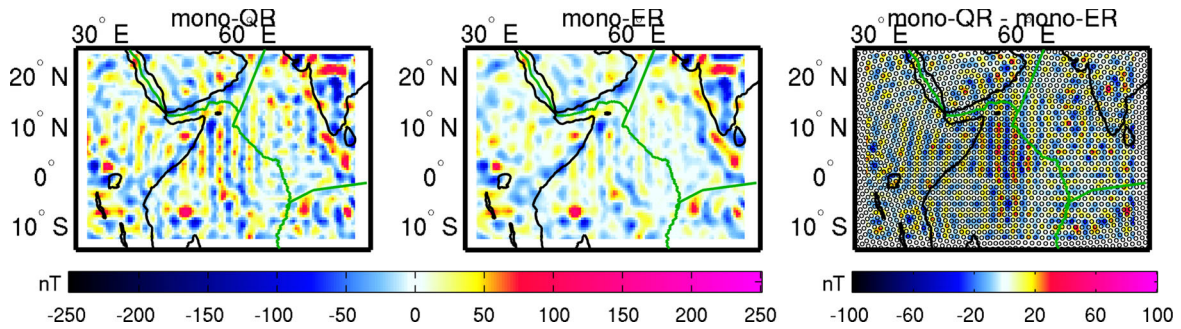


Figure 9. Lithospheric radial magnetic field at the Earth's surface for mono-QR with $\lambda = 928 \text{ nT}^{-2}$, mono-ER with $\lambda = 4640 \text{ nT}^{-2}$ and $\omega = 25 \times 10^{-4} \text{ nT}$ and the corresponding differences. The illustrated region corresponds to the northwest area of the Indian ocean. Additionally, the individual source locations are indicated by the black circles in the right panel of the figure.

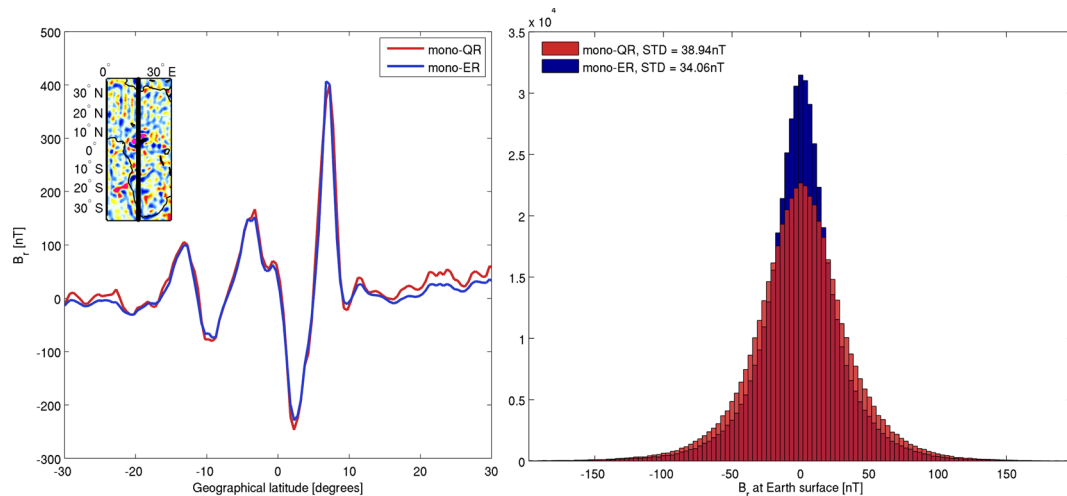


Figure 10. Left: model prediction for the radial lithospheric magnetic field at the Earth's surface (on a $0.5^\circ \times 0.5^\circ$ grid) along an orbital profile at longitude $\phi = 17.25^\circ$ crossing the Bangui magnetic anomaly (inserted figure). The result is given for mono-QR (red) and mono-ER (blue) models. Right: histogram comparing the global statistics of the modelled lithospheric radial magnetic field at the Earth's surface predicted by mono-QR (red) and mono-ER (blue). The corresponding surface locations are identical to monopole locations for a grid refinement level $L = 7$. Standard deviation values are given in the upper part of the figure.

Next we move on to consider the models derived using the maximum entropy regularization (ER) approach. ER models were derived applying the same regularization parameters as in Fig. 3 and using the respective QR solutions as the starting models. The entropy default parameter ω was initially set to a large value and then gradually decreased ensuring model convergence at each step. The presented values of ω are the minimum values for which we were able to obtain numerical convergence. Fig. 5 shows the power spectra for both the ER and QR models. As expected, the ER approach enhances local magnetic field amplitudes, resulting in slightly larger power at higher spherical harmonic degrees compared to QR models with the same λ . We found it advantageous to have a starting model with a minimum amount of noise mapped into the monopole sources. Our preferred ER model is therefore based on the largest investigated regularization parameter $\lambda = 4640 \text{ nT}^{-2}$ and $\omega = 25 \times 10^{-4} \text{ nT}$. Henceforth, this model will be referred to as 'mono-ER'. The lower part of Fig. 4 illustrates the corresponding radial lithospheric field map at the Earth's surface. It is noteworthy that the oceanic regions are generally of lower amplitude in mono-ER compared to mono-QR (the mean value of the absolute radial field magnitude in the oceanic regions is 3.22 nT lower in mono-ER than in mono-QR), while over large continental anomalies the amplitude in mono-ER can be higher (left panel of Fig. 10 for $\sim 8^\circ$ north). The global and local differences between mono-QR

and mono-ER are presented in Figs 8 and 9, respectively. The differences are globally distributed, with the largest values in the polar regions, around large local lithospheric field anomalies and in some specific oceanic regions (e.g. in the mid-Atlantic, north of Brazil and the Indian ocean). The right panel of Fig. 9 shows an example of the local differences between mono-QR and mono-ER models as well as monopole locations projected to the surface of the Earth. Model differences are generally of larger scale than the distance between individual sources.

Comparing the statistics for the mono-QR and mono-ER models (see Tables 2 and 3) we were able to arrive a very similar model misfit (difference < 0.1 per cent). This is surprising since mono-ER has much less power at high degree (Fig. 5) with which to fit observations to the same level as mono-QR.

Fig. 6 presents the degree correlation between MF7 and the models mono-QR, mono-ER and CM5. The mono-QR and mono-ER models are well correlated ($\rho > 0.7$) with MF7 up to SH degree $n = 100$, while this value is slightly larger for the correlation between MF7 and CM5 ($n = 108$). Fig. 6 also shows that the mono-QR and mono-ER models are themselves well correlated out to at least degree 120 (light blue curve).

Another illustration of the differences between models mono-QR and mono-ER is shown in Fig. 7. After transforming the model results to the SH domain, the Gauss coefficient differences are here

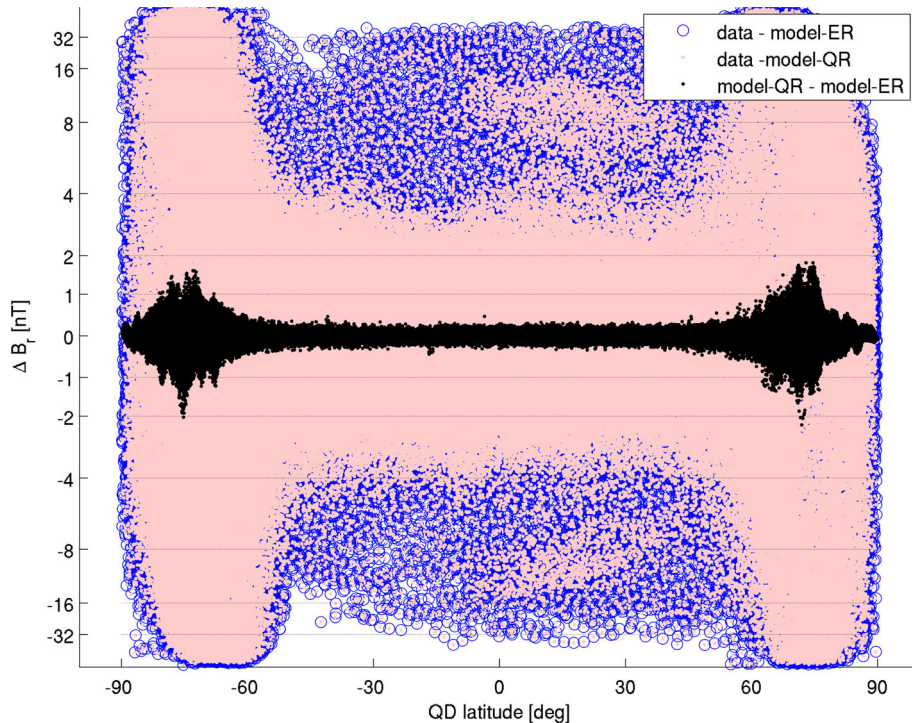


Figure 11. Radial field residuals between the CHAMP data and the mono-QR (red) and mono-ER (blue) models. Differences between the models are shown in black. The y-axis is nonlinear and proportional to $\frac{8}{\pi} \arctan(y/5)$ nT in order to emphasize near-zero values.

considered in a degree/order plot. The differences are normalized by the mean spectral amplitude of the MF7 coefficients according to eq. (9). The models start to differ notably above SH degree 60, partly because there is then much less power in the mono-ER compared with the mono-QR model. However, even at higher degree, the differences remain relatively small, in the range of 10 per cent. We attribute the differences between mono-QR and mono-ER shown here primarily to the applied regularization. Additionally, interesting vertical stripes are observed especially between degrees 60 and 95 in Fig. 7. These features are due to north–south directed structures which are especially seen in the oceanic regions of Fig. 4, being most prominent in model-QR (Fig. 9).

The right part of Fig. 10 presents the global surface radial magnetic field distribution of mono-QR and mono-ER by means of a histogram. The corresponding surface grid locations are identical to the monopole source locations for a grid refinement level $L = 7$. It illustrates that the mono-ER model predicts more field values closer to zero compared to the QR counterpart, while at the same time the ER model still allows larger field amplitudes where locally required by the data. The latter point is best appreciated by considering the maximum and minimum global radial field values, which are 577 nT and -893 nT for mono-QR and 727 nT and -1078 nT for mono-ER (note that the long tails of the mono-ER distribution are difficult to see in Fig. 10 due to the scale). In statistical terminology, the ER approach follows a more Laplacian distribution, as expected for crustal field anomalies (Walker & Jackson 2000).

The left part of Fig. 10 shows the surface radial magnetic field values along a constant longitude crossing the Bangui anomaly. Despite the similar morphology of the anomalies, the mono-ER model has smaller field amplitudes in regions with weak magnetic anomalies and sometimes has larger amplitudes than the mono-QR model over the large magnetic anomalies.

Fig. 11 illustrates the derived model residuals for mono-QR and mono-ER with respect to the corresponding QD latitudes. Differences between the individual model values are shown in black and emphasize the very similar model predictions as already seen in the previous figures as well as Tables 2 and 3.

We also derived the model resolution matrices for mono-QR and mono-ER. From the respective traces we found the number of degrees of freedom for models mono-QR and mono-ER to be 11635 and 9515, respectively, that is, mono-ER is able to obtain almost the same fit to the observations as mono-QR but with almost 20 per cent fewer effective degrees of freedom.

Overall we find that, compared to traditional SH models and the mono-QR model, the mono-ER model requires a smaller number of degrees of freedom to achieve the same level of fit to the observations and possesses Laplacian statistics with a small number of anomalies of high amplitude and many regions with very weak anomalies. The latter corresponds well with the lithospheric field expectations based on satellite, airborne and marine data (Thébault *et al.* 2010).

6 CONCLUSIONS AND OUTLOOK

We have presented a new method for modelling the global lithospheric magnetic field at the Earth's surface based on an icosahedral grid of equivalent monopole sources. We obtained model solutions by iterative least squares, with Huber weighting of misfit values and latitude-dependent data uncertainties implemented for all three vector field components at all latitudes. The approach was tested using CHAMP satellite data spanning the period 2009–2010.

Both QR and ER approaches based on monopole modelling were investigated. The former involves minimizing the Euclidean norm of the model parameters, while the maximum entropy approach minimizes an information-based measure of complexity.

The obtained model results have been compared statistically and by looking at the corresponding radial magnetic field values globally and locally at the Earth's surface. The preferred mono-QR and mono-ER models show very similar misfits, but the ER approach allows for larger lithospheric magnetic field values locally where there are strong anomalies, while at the same time favouring weaker values in oceanic regions in agreement with geological expectations. Furthermore, the mono-ER model has a much smaller number of degrees of freedom. The derived models correlate satisfactorily with MF7 up to SH degree $n = 100$.

The method does not involve spherical harmonics and is therefore also suitable for local geomagnetic field investigations with higher resolution. Nonetheless, whenever needed, the equivalent source model parameters can easily be transformed into spherical harmonics. Interestingly, eqs (5) to (6) can be used to produce spherical harmonic models and power spectra specifically for regions of interest, by retaining only the equivalent sources inside that region, and implicitly setting the amplitude of the remaining sources to zero. Note that the R-SCHA (Thébault & Vervelidou 2015) and spherical Slepian function (Beggan *et al.* 2013) approaches can also be used to derive local power spectra.

Future applications will make use of *Swarm* data in combination with high-resolution aeromagnetic measurements. For the latter, local refinement of the monopole grid will be implemented in the modelling approach.

Extending the method to also handle field differences, approximating gradients, along and across satellite tracks (Kotsiaros *et al.* 2015; Olsen *et al.* 2015) should lead to further improvements of the lithospheric field models, but this will require a more sophisticated treatment of the data covariance matrix $\underline{\underline{C}}$.

ACKNOWLEDGEMENTS

The authors are grateful for the comments of the editor Prof Gary Egbert, the reviewer Dr Mike Purucker and an anonymous reviewer, who helped to improve the manuscript and clarify the mathematical presentation. Support by the Research Council of Norway through the Petromaks programme, by ConocoPhillips and Lundin Norway, and by the Technical University of Denmark is highly appreciated. The support of the CHAMP mission by the German Aerospace Center (DLR) and the Federal Ministry of Education and Research is gratefully acknowledged.

REFERENCES

- Arkani-Hamed, J., Langel, R.A. & Purucker, M., 1994. Scalar magnetic anomaly maps of Earth derived from POGO and Magsat data, *J. geophys. Res.*, **99**(B12), 24 075–24 090.
- Baumgardner, J.R. & Frederickson, P.O., 1985. Icosahedral discretization of the two-sphere, *SIAM J. Numer. Anal.*, **22**(6), 1107–1115.
- Beggan, C.D., Saarimäki, J., Whaler, K.A. & Simons, F.J., 2013. Spectral and spatial decomposition of lithospheric magnetic field models using spherical slepian functions, *Geophys. J. Int.*, **193**(1), 136–148.
- Blakely, R., 1996. *Potential Theory in Gravity and Magnetic Applications*, Cambridge Univ. Press.
- Bloxham, J., Gubbins, D. & Jackson, A., 1989. Geomagnetic secular variation, *Phil. Trans. R. Soc. Lond., A*, **329**, 415–502.
- Chambodut, A., Panet, I., Manda, M., Diament, M., Holschneider, M. & Jamet, O., 2005. Wavelet frames: an alternative to spherical harmonic representation of potential fields, *Geophys. J. Int.*, **163**(3), 875–899.
- Connerney, J. *et al.*, 1999. Magnetic lineations in the ancient crust of Mars, *Science*, **284**(5415), 794–798.
- Constable, C., 1988. Parameter estimation in non-Gaussian noise, *Geophys. J. Int.*, **94**(1), 131–142.
- Covington, J., 1993. Improvement of equivalent source inversion technique with a more symmetric dipole distribution model, *Phys. Earth planet. Inter.*, **76**(3), 199–208.
- Driessen, K. & Rombouts, R., 2007. *Matlab Library for Robust Analysis*, Available at: <http://wis.kuleuven.be/stat/robust.html>.
- Emmert, J., Richmond, A. & Drob, D., 2010. A computationally compact representation of Magnetic-Apex and Quasi-Dipole coordinates with smooth base vectors, *J. geophys. Res.*, **115**(A8), doi:10.1029/2010JA015326.
- Gillet, N., Jackson, A. & Finlay, C.C., 2007. Maximum entropy regularization of time-dependent geomagnetic field models, *Geophys. J. Int.*, **171**(3), 1005–1016.
- Gull, S. & Skilling, J., 1999. *Quantified Maximum Entropy - MemSys5 Users' Manual, Version 1.2*, Maximum Entropy Data Consultants Ltd.
- Haines, G., 1985. Spherical cap harmonic analysis, *J. geophys. Res.*, **90**(B3), 2583–2591.
- Hansen, P.C., 1998. *Rank-deficient and Discrete Ill-posed Problems: Numerical Aspects of Linear Inversion*, vol. 4, SIAM.
- Huber, P.J., 1964. Robust estimation of a location parameter, *Annals of Mathematical Statistics*, **35**(1), 73–101.
- Inglis, T., 1987. *Petroleum Engineering and Development Studies, Vol. 2: Directional Drilling*, Graham & Trotman.
- Jackson, A., Constable, C. & Gillet, N., 2007. Maximum entropy regularization of the geomagnetic core field inverse problem, *Geophys. J. Int.*, **171**(3), 995–1004.
- Kotsiaros, S., Finlay, C.C. & Olsen, N., 2015. Use of along-track magnetic field differences in lithospheric field modelling, *Geophys. J. Int.*, **200**(2), 878–887.
- Langel, R. & Whaler, K., 1996. Maps of the magnetic anomaly field at Earth's surface from scalar satellite data, *Geophys. Res. Lett.*, **23**(1), 41–44.
- Langel, R.A. & Hinze, W.J., 1998. *The Magnetic Field of the Earth's Lithosphere: The Satellite Perspective*, Cambridge Univ. Press.
- Langlais, B., Purucker, M. & Manda, M., 2004. Crustal magnetic field of Mars, *J. geophys. Res.*, **109**(E2), doi:10.1029/2003JE002048.
- Lesur, V., Rother, M., Vervelidou, F., Hamoudi, M. & Thébault, E., 2013. Post-processing scheme for modelling the lithospheric magnetic field, *Solid Earth*, **4**, 105–118.
- Loves, F., 1974. Spatial power spectrum of the main geomagnetic field, and extrapolation to the core, *Geophys. J. R. astr. Soc.*, **36**(3), 717–730.
- Maisinger, K., Hobson, M.P. & Lasenby, A., 2004. Maximum-entropy image reconstruction using wavelets, *Mon. Not. R. astr. Soc.*, **347**(1), 339–354.
- Maus, S., 2010. *Magnetic Field Model MF7*, Available at: <http://geomag.org/models/MF7.html>.
- Maus, S., Yin, F., Lühr, H., Manoj, C., Rother, M., Rauberg, J., Michaelis, I., Stolle, C. & Müller, R., 2008. Resolution of direction of oceanic magnetic lineations by the sixth-generation lithospheric magnetic field model from champ satellite magnetic measurements, *Geochem. Geophys. Geosyst.*, **9**(7), doi:10.1029/2008GC001949.
- Mayer, C. & Maier, T., 2006. Separating inner and outer Earth's magnetic field from CHAMP satellite measurements by means of vector scaling functions and wavelets, *Geophys. J. Int.*, **167**(3), 1188–1203.
- Menke, W., 2012. *Geophysical Data Analysis: Discrete Inverse Theory*, Academic press.
- Molnar, P., 1988. Continental tectonics in the aftermath of plate tectonics, *Nature*, **335**(6186), 131–137.
- Ness, N.F., 1979. The magnetic fields of Mercury, Mars, and Moon, *Annu. Rev. Earth Planet. Sci.*, **7**, 249–288.
- O'Brien, M.S. & Parker, R.L., 1994. Regularized geomagnetic field modelling using monopoles, *Geophys. J. Int.*, **118**(3), 566–578.
- Olsen, N., 2002. A model of the geomagnetic field and its secular variation for epoch 2000 estimated from Ørsted data, *Geophys. J. Int.*, **149**(2), 454–462.
- Olsen, N. *et al.*, 2005. *Swarm end-to-end mission performance simulator study*, DSRI Report 1/2004, ISSN 1602-527X.
- Olsen, N., Lühr, H., Sabaka, T., Manda, M., Rother, M., Tøffner-Clausen, L. & Choi, S., 2006. CHAOS - a model of the Earth's magnetic field derived

- from CHAMP, Ørsted, and SAC-C magnetic satellite data, *Geophys. J. Int.*, **166**(1), 67–75.
- Olsen, N., Lühr, H., Finlay, C.C., Sabaka, T.J., Michaelis, I., Rauberg, J. & Tøffner-Clausen, L., 2014. The CHAOS-4 geomagnetic field model, *Geophys. J. Int.*, **197**(2), 815–827.
- Olsen, N. *et al.*, 2015. The swarm initial field model for the 2014 geomagnetic field, *Geophys. Res. Lett.*, **42**(4), 1092–1098.
- Plado, J., Pesonen, L., Koeberl, C. & Elo, S., 2000. The Bosumtwi meteorite impact structure, Ghana: a magnetic model, *Meteorit. Planet. Sci.*, **35**(4), 723–732.
- Purucker, M.E. & Nicholas, J.B., 2010. Global spherical harmonic models of the internal magnetic field of the Moon based on sequential and coestimation approaches, *J. geophys. Res.*, **115**(E12), doi:10.1029/2010JE003650.
- Richmond, A., 1995. Ionospheric electrodynamics using magnetic apex coordinates, *J. Geomag. Geoelectr.*, **47**(2), 191–212.
- Sabaka, T.J. & Olsen, N., 2006. Enhancing comprehensive inversions using the Swarm constellation, *Earth Planets Space*, **58**(4), 371–395.
- Sabaka, T.J., Olsen, N., Tyler, R.H., Kuvshinov, A., Sabaka, T.J., Olsen, N., Tyler, R.H. & Kuvshinov, A., 2015. CM5, a pre-Swarm comprehensive geomagnetic field model derived from over 12 yr of CHAMP, Ørsted, SAC-C and observatory data, *Geophys. J. Int.*, **200**(3), 1596–1626.
- Stockmann, R., Finlay, C.C. & Jackson, A., 2009. Imaging Earth's crustal magnetic field with satellite data: a regularized spherical triangle tessellation approach, *Geophys. J. Int.*, **179**, 929–944.
- Thébault, E., 2006. Global lithospheric magnetic field modelling by successive regional analysis, *Earth Planets Space*, **58**(4), 485–495.
- Thébault, E., 2008. A proposal for regional modelling at the Earth's surface, R-SCHA2D, *Geophys. J. Int.*, **174**(1), 118–134.
- Thébault, E. & Vervelidou, F., 2015. A statistical power spectrum of the Earth's lithospheric magnetic field, *Geophys. J. Int.*, **201**, 605–620.
- Thébault, E., Purucker, M., Whaler, K.A., Langlais, B. & Sabaka, T.J., 2010. The magnetic field of the Earth's lithosphere, *Space Sci. Rev.*, **155**(1–4), 95–127.
- Torge, W., 2001. *Geodesy*, Walter de Gruyter.
- Toyoshima, M., Shibuya, H., Matsushima, M., Shimizu, H. & Tsunakawa, H., 2008. Equivalent source mapping of the lunar crustal magnetic field using ABIC, *Earth Planets Space*, **60**(4), 365–373.
- Walker, M. & Jackson, A., 2000. Robust modelling of the Earth's magnetic field, *Geophys. J. Int.*, **143**, 799–808.
- Whaler, K. & Purucker, M., 2005. A spatially continuous magnetization model for Mars, *J. geophys. Res.*, **110**(E9), doi:10.1029/2004JE002393.

APPENDIX: GREEN'S MATRIX COMPONENTS

The Green's matrix $\underline{\underline{G}}$ represents the linear relationship between the magnetic monopole sources \mathbf{q} and the corresponding lithospheric magnetic field \mathbf{B} ,

$$\begin{aligned} \mathbf{B} &= \underline{\underline{G}}\mathbf{q} \\ B_{i,p} &= -\sum_{k=1}^K q_k \left[\hat{\mathbf{e}}_{i,p} \cdot \nabla_p \frac{r_k^2}{r_{ik}} \right] \\ &= \sum_{k=1}^K q_k g_{ik,p} \end{aligned} \quad (\text{A1})$$

where i and k represent a given lithospheric magnetic field prediction and the equivalent source index, respectively.

The general formula for a given element p (for $p = r, \theta$ or ϕ) of the Green's matrix is

$$\underline{\underline{G}}_p = g_{ik,p} = -\hat{\mathbf{e}}_{i,p} \cdot \nabla_p \frac{r_k^2}{r_{ik}}. \quad (\text{A2})$$

Then

$$\begin{aligned} g_{ik,r} &= -\frac{\partial}{\partial r_i} \left(\frac{r_k^2}{r_{ik}} \right) \\ &= \frac{r_k^2}{r_{ik}^3} [r_i - r_k \cos(\mu_{ik})] \\ g_{ik,\theta} &= -\frac{1}{r_i} \frac{\partial}{\partial \theta_i} \left(\frac{r_k^2}{r_{ik}} \right) \\ &= \frac{r_k^3}{r_{ik}^3} [\sin(\theta_i) \cos(\theta_k) - \cos(\theta_i) \sin(\theta_k) \cos(\phi_i - \phi_k)] \\ g_{ik,\phi} &= -\frac{1}{r_i \sin(\theta_i)} \frac{\partial}{\partial \phi_i} \left(\frac{r_k^2}{r_{ik}} \right) \\ &= \frac{r_k^3}{r_{ik}^3} [\sin(\theta_k) \sin(\phi_i - \phi_k)]. \end{aligned} \quad (\text{A3})$$